Effect of temperature and strain rate on the deformation behavior of Ti5321 during hot-compression

Gu, B.; Chekhonin, P.; Xin, S. W.; Liu, G. Q.; Ma, C. L.; Zhou, L.; Skrotzki, W.;

Originally published:

April 2021

Journal of Alloys and Compounds 876(2021), 159938

DOI: https://doi.org/10.1016/j.jallcom.2021.159938

Perma-Link to Publication Repository of HZDR:

https://www.hzdr.de/publications/Publ-32620

Effect of temperature and strain rate on the deformation behavior of Ti5321 during hot-compression

B. Gu[1,2,*], P. Chekhonin[3], S.W. Xin[4], G. Q. Liu[5], C.L. Ma[1,*], L. Zhou[1,4], W. Skrotzki[2]

[1] Key Laboratory of Aerospace Advanced Materials and Performance of Ministry of Education, School of Materials Science and Engineering, Beihang University, Beijing 100191, China
[2] Institute of Solid State and Materials Physics, Dresden University of Technology, 01062 Dresden, Germany
[3] Helmholtz-Zentrum Dresden-Rossendorf, 01328 Dresden, Germany
[4] Northwest Institute for Nonferrous Metal Research, Xi'an 710016, China
[5] School of Mechanical Engineering and Automation, Beihang University, Beijing 100191, China

Abstract

The effect of deformation temperature and strain rate (collectively described by the Zener-Hollomon parameter *Z*) on the deformation mechanism and texture formation of the metastable β-titanium alloy Ti5321 across the β-transus temperature during hot-compression was investigated by electron backscatter diffraction. In the β-phase field, it is found that the deformation behavior and texture formation varies depending on *Z*. With decreasing *Z* dynamic recovery and dynamic recrystallization become more and more important. The activation energy for steady state deformation is 240 kJ/mol and 370 kJ/mol in the β- and (α+β)-phase field, respectively. The texture developed is a <100> <111> double-fiber with <100> dominating at all deformation conditions. The <111> fiber gets more prominent with increasing *Z* suggesting that it is mainly related to deformation. Flow softening behavior of Ti5321 is associated with dynamic globularization of the α-phase and promotion of β-grain formation by continuous dynamic recrystallization.

* Corresponding author:

E-mail: gubin_buaa@hotmail.com (B.Gu)

* Corresponding author:

E-mail: machaoli@buaa.edu.cn (C.L. Ma)

Keywords: Metastable β-titanium alloy, EBSD, microstructure, texture, dynamic recrystallization, deformation mechanism

1. Introduction

Metastable β-titanium alloys are attractive materials for aerospace application due to their high strength and good workability [1-4]. Their mechanical properties are very sensitive to thermo-mechanical processing (TMP) which in a targeted manner allows adjusting microstructure and texture [5-7]. In order to not only relying on empirical optimization of TMP, it is important to have a fundamental understanding of the relationship between processing variables, microstructure, texture and corresponding deformation behavior. Generally, TMP through deformation temperature and strain rate affects the deformation behavior with respect to work-hardening and dynamic recovery (DRV) as well as dynamic recrystallization (DRX) leading to flow softening [1, 8]. While work-hardening of metastable β-Ti alloys has not been reported frequently, flow softening has been found in titanium alloys, such as Ti-5Al-5V-5Mo-3Cr (Ti5553) and Ti-7Mo-3Nb-3Cr-3Al (Ti7333), when deformed in the subtransus region [9-11]. The flow softening was correlated with adiabatic heating and dynamic precipitation of the α-phase [12]. In a variety of alloys, DRX is one of the most promising mechanisms for grain refinement [13]. DRX can be classified into discontinuous dynamic recrystallization (DDRX) and continuous dynamic recrystallization (CDRX) [8, 14, 15, 16]. During DDRX, which is taking place at elevated temperatures, new grains evolve by nucleation and growth [14]. On the other hand, CDRX with increasing strain is characterized by a gradual transformation of low angle boundaries (LAGBs) into high angle grain boundaries (HAGBs) [13, 14]. CDRX was found during compression of Ti-5Al-5Mo-

5V-3Cr-1Zr (Ti55531) at comparatively high strain rates and strains above 50% [17, 18]. Zhao et al. [19] verified CDRX in Ti-10V-2Fe-3Al (Ti1023) by progressive lattice rotation from the center to the edge of deformed grains.

In addition, deformation temperature and strain rate, conveniently described by the Zener-Hollomon parameter *Z*, affect mechanisms of deformation and DRX, i.e. microstructure and texture formation [16, 20, 21]. DRX has been found for ln $Z < 21$ in Ti-15V-3Cr-3Sn-3Al (Ti153) with the volume fraction of DRX increasing with decreasing *Z* [22]. CDRX has also been observed in Ti1023 at high strain rates and low temperatures (high *Z* value) [19]. Regarding texture formation, it was reported that during rolling of aluminum alloys the stability of the texture components {011}<211> ("Brass") and {100}<100> ("Cube") increases as *Z* decreases [20]. In γ-TiAl a sharp fiber texture develops during compression at low *Z* conditions, while in nickel and copper after DRX the opposite has been observed [16]. However, in titanium alloys studies on the *Z* dependency of texture during hot compression are still very limited.

Therefore, it is the aim of the present investigation to systematically study the deformation behavior and texture formation in Ti5321 during hot-compression in the β- and (α+β)-phase field under the influence of deformation temperature and strain rate. This metastable β-Ti alloy with nominal composition of Ti-5Al-3V-3Mo-2Cr-2Zr-1Nb-1Fe (wt.%) has been recently developed [23, 24]. It exhibits an excellent combination of strength and fracture toughness. These properties are suitable for large-scale structural applications in aerospace [23]. The study of microstructure and texture evolution and related deformation behavior can be used to optimize TMP of Ti5321.

2. Experimental

The metastable Ti5321 alloy used was produced by the Northwest Institute for Nonferrous Metal Research in China by bar-rolling in the (α+β)-phase field. According to the chemical

analysis performed in [23] with inductively coupled plasma - atomic emission spectrometry (ICP-AES) the composition of the ingot alloy is given as: Ti-5.02Al-3.03Mo-2.99V-2.06Cr-2.01Zr-1.37Nb-0.99Fe-0.004N-0.0011H-0.064O, in wt.%. The β-transus temperature (T_β) of the alloy measured by the metallographic method is (1128 ± 5) K [23, 24]. Prior to compression the specimens were solution-treated (ST) at 1173 K for 1 h followed by water quenching.

Hot-compression tests were conducted on a Gleeble-3800 thermomechanical simulator using cylindrical samples with 12 mm height and 8 mm diameter. In order to minimize friction, all the sides of the samples were mechanically grinded. A thermocouple welded at mid span of the specimens was used to control and measure the processing temperature. In order to further reduce friction and keep the deformation uniform, thin tantalum sheets were placed between compression specimen and dies. The compressive tests were performed at initial strain rates of 1 s^{-1}, 0.1 s^{-1} and 0.01 s^{-1} to an engineering strain of 60% (in the following just called strain) at temperatures between 1023 K and 1223 K with an interval of 50 K. Below T_β at 1023 K, 1073 K and 1103 K, before compression the samples were held at the corresponding temperature for 2 min in order to form more α-platelets. As soon as the deformation was finished, the samples were water-quenched to retain the high temperature deformation microstructure. All compression tests were performed in vacuum.

The investigation of the microstructure was carried out through electron backscatter diffraction (EBSD) in a Zeiss ULTRA 55 scanning electron microscope (SEM). In order to achieve the surface quality required for EBSD examinations, specimens were prepared by conventional grinding (final step: wet SiC-paper 4000 grid), and electropolishing in a solution of one part perchloric acid (70 vol.%) and nine parts of ethanol using a voltage of 40 V for 40 s while keeping the electrolyte at –14°C.

The EBSD mappings were performed at an operating voltage between 10 kV and 20 kV. A step size of 3 μm was applied to collect data over large areas; a smaller step size of 80 nm

was used for detailed analyses. The EBSD maps were always taken with the compression axis (CA) parallel to the SEM image vertical (SEM Y) and the radial direction (RD) parallel to the SEM image horizontal (SEM X). For the calculation of inverse pole figure (IPF) maps the EBSD data were rotated by 90° about the radial direction (RD). Thus, coloring of IPF maps is with respect to CA. Pole figures (PFs) were also calculated from the EBSD data, viewed from the denoted plane CA-RD. To ensure the accuracy of each PF with regard to grain statistics, at least two EBSD mappings were carried out so that in total more than 1000 grains were included. The data acquisition and analysis was carried out using HKL Channel 5 EBSD software. The texture of the β-phase below T_β was separated by removing the α-phase orientation data from the EBSD mapping. The volume fractions of texture fibers (15° orientation spread) were calculated using HKL Channel 5 EBSD software. The grain size was determined by the line intercept method of HKL Channel 5 EBSD software. Recrystallized grains were identified through the grain orientation spread (GOS) method. GOS is defined as the average deviation in orientation between each point inside a grain and the average orientation of the grain [25]. Internal misorientation within grains is one of factors showing strain distribution and stored energy [25-27]. A high GOS value indicates a relatively high density of dislocations, i.e. high amount of stored energy, whereas recrystallized areas are characterized by relatively low dislocation density and a low GOS value. A grain is considered as recrystallized for GOS less than 2°.

The micro-hardness at room temperature (RT) was tested by a Vickers hardness tester applying a load of 300 gf for 15 s. Ten tests were conducted for each condition, the average values are presented.

3. Results

3.1. Initial microstructure

The ST Ti5321 is fully recrystallized and consists of equiaxed grains with an average size of

165 µm (Fig. 1 a). As shown by the {100} and {111} PFs in Fig. 1b extracted from three EBSD maps including about 500 β-grains, the ST Ti5321 bars do not exhibit a particular texture. Due to the limited statistics of EBSD with respect to texture, the peaks visible in the PFs can be attributed to few large grains. Therefore, the authors assume that at this stage the bars had an almost random texture.

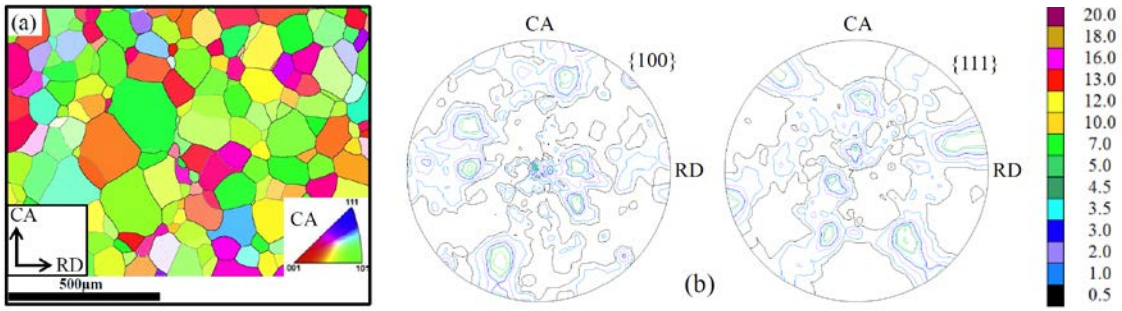

Fig. 1: (a) EBSD mapping in the CA-RD plane plotted as CA-IPF after 1 h solution-treatment at 1173 K and water-quenching to room temperature (ST state); (b) corresponding {100} and {111} PFs of the β-phase.

3.2. Flow behavior

Figure 2 presents the compression flow curves of Ti5321 at different temperatures and strain rates. Generally, the flow stress decreases with increasing temperature and decreasing strain rate. The true stress - true strain curves can be subdivided into three different trends indicating different deformation mechanisms depending on deformation temperature and strain rate:

(i) Above T_β, the flow curves show work-hardening behavior at the highest strain rate of 1 s^{-1}, which is rarely observed in other β-Ti alloys, including Ti55531 [17, 18], Ti1023 [19] and Ti5553 [10].

(ii) The flow curves for 0.01 s^{-1} above 1073 K show a discontinuous yielding followed by steady state flow.

(iii) Below T_β, the flow curves exhibit flow softening behavior. The extent of flow softening increases with decreasing temperature.

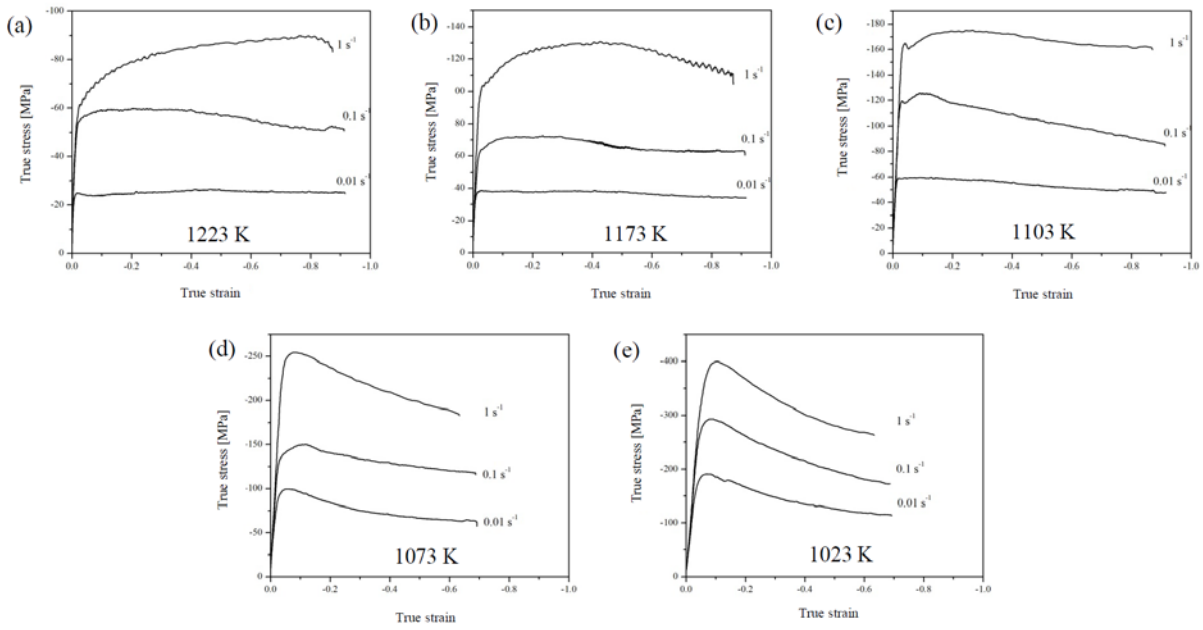

Fig. 2: True stress – true strain curves of Ti5321 compressed at different temperatures and strain rates.

3.3. Constitutive relationships

During stationary hot-deformation flow stress σ, strain rate $\dot{\varepsilon}$ and deformation temperature T are interrelated according to the constitutive equation [28]:

$$\dot{\varepsilon} = A[\sinh(c\sigma)]^n e^{\left(\frac{-Q}{RT}\right)}, \quad (1)$$

with Q activation energy, R gas constant, n stress exponent, A and c material constants. At low stresses, eq. (1) reduces to the commonly used power-law relationship [28]:

$$\dot{\varepsilon} = A\sigma^n e^{\left(\frac{-Q}{RT}\right)}, \quad (2)$$

For constant temperature, this can be checked by a double-logarithmic plot (eq. (3))

$$\ln\dot{\varepsilon} = A - \frac{Q}{RT} + n\ln\sigma. \quad (3)$$

In the case of a linear dependency n is given by the slope (Fig. 3). Above T_β n ≈ 3.7, below it is increasing to 5.6.

For σ = const, Q is obtained from the slope of the Arrhenius plot of strain rate against

reciprocal deformation temperature (Fig. 4). Below and above T_β the activation energies are 370 kJ/mol and 240 kJ/mol, respectively. The Q value obtained in the (α+β)-phase field is higher than those reported for alloys Ti1023 (294 kJ/mol) [29], Ti55531 (275 kJ/mol) [18] and Ti5553 (183 kJ/mol) [2]. The Q value obtained in the β-phase field is higher than that of self-diffusion in pure Ti β-phase (153 kJ/mol) [30].

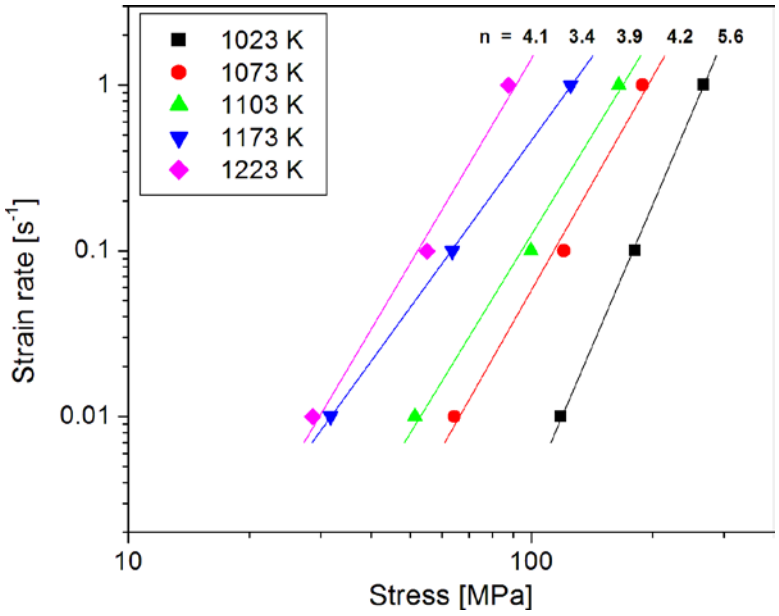

Fig. 3: Strain rate as a function of stress at 60% strain according to eq. (3) for different temperatures.

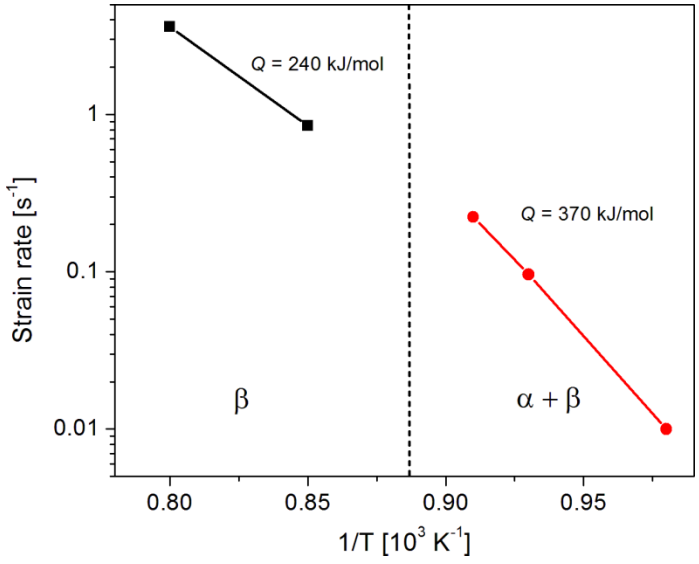

Fig. 4: Arrhenius plot for determination of the activation energy in the β- and (α+β)-phase field. Strain rates are taken from Fig. 3 at a stress of 118 MPa.

3.4. Microstructure and texture evolution

During hot-deformation the microstructure and texture evolution with strain depends on deformation temperature and strain rate. These deformation parameters are often combined to a single parameter, the Zener-Hollomon parameter *Z*, which is defined as

$$Z = \dot{\varepsilon} e^{\frac{Q}{RT}} . \quad (4)$$

Figure 5 shows the EBSD results of the samples compressed at different temperatures and strain rates to a strain of 60%. For all conditions ln *Z* is also given. Figure 6 provides details of the hot-deformation microstructure. In comparison to the initial microstructure (Fig. 1), a change of morphology and orientation of grains after hot-compression at 1023 K to 1223 K is evident.

After deformation at 1103 K, 1173 K and 1223 K, at the highest strain rate of 1 s^{-1}, the grain boundaries are almost straight (Figs. 5 and 6), and a subgrain structure forms within prior existing grains. At lower strain rates, the grain boundaries become more and more serrated. Above T_β at high strain rate (1 s^{-1}), subgrains form at the rim of prior existing grains, whereas when the strain rate decreases to 0.01 s^{-1} the deformation leads to a more uniform distribution of LAGBs (Fig. 6). With increasing deformation temperature the grain boundaries also become more and more serrated. After deformation below T_β the grain boundaries are no longer serrated for any strain rate.

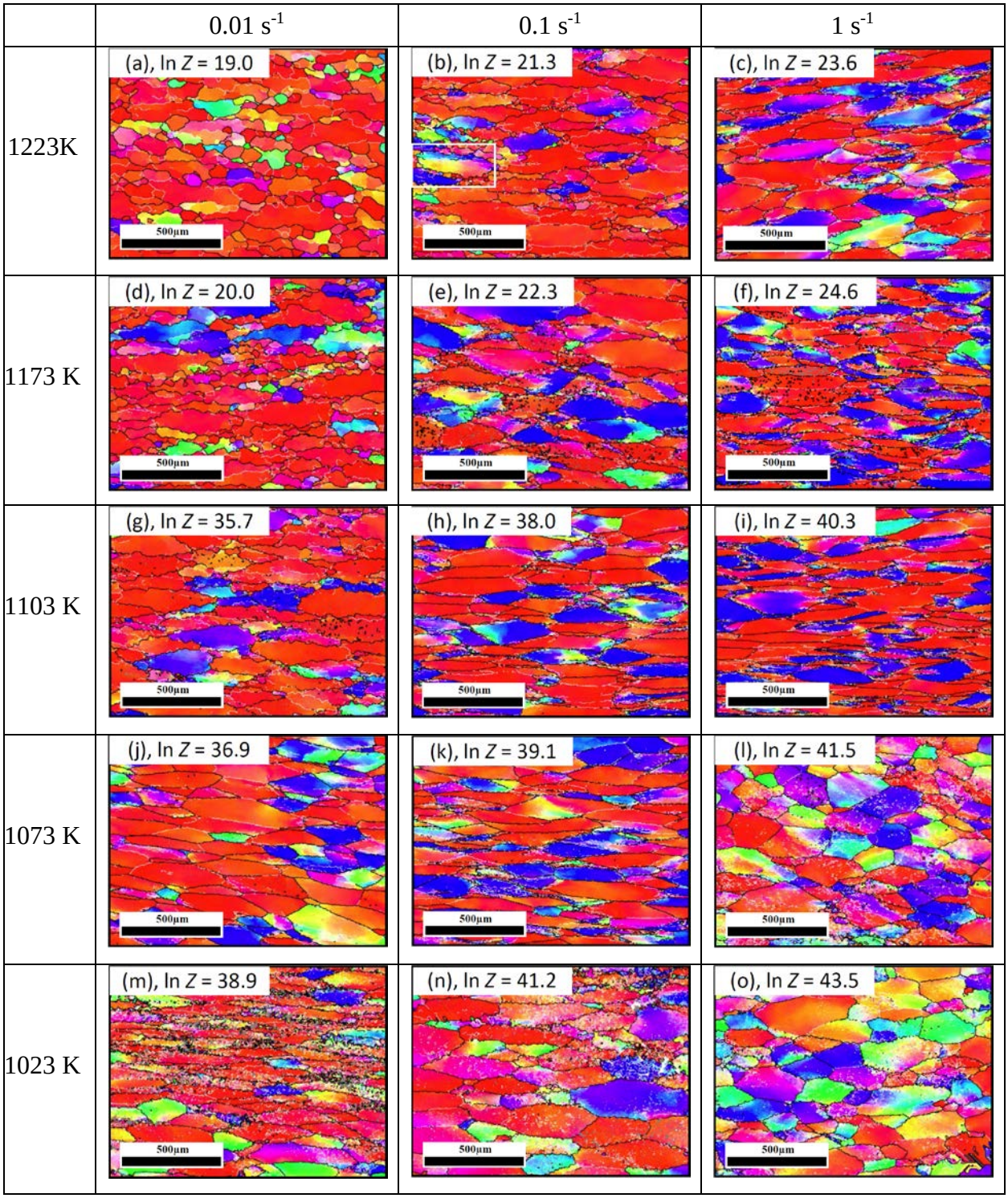

Fig. 5: EBSD CA-IPF maps of Ti5321 hot-compressed at different strain rates and temperatures, respectively ln *Z*. The grains are colored according to a standard color code presented as an IPF with respect to CA. LAGBs with misorientations from 3° to 15° are colored in white, HAGBs with misorientations larger than 15° in black. (sample reference system as in Fig. 1)

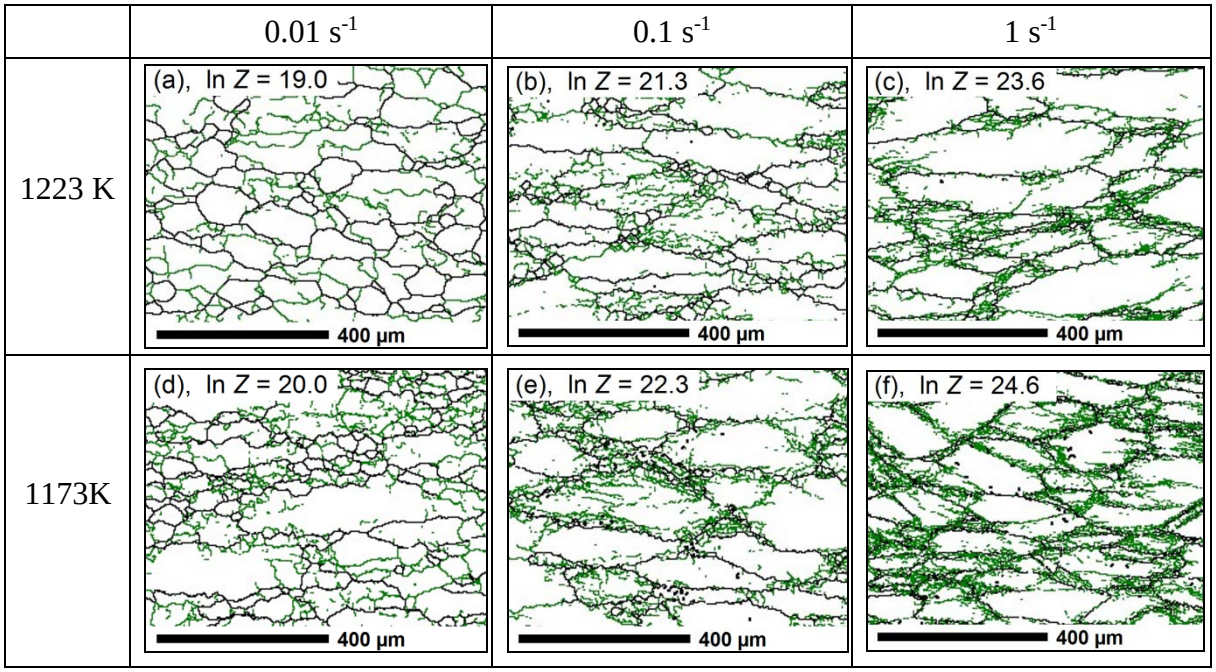

Fig. 6: EBSD grain boundary maps (HAGBs in black and LAGBs in green) in samples deformed at different strain rates and temperatures, respectively ln *Z*. (sample reference system as in Fig. 1)

Below T_β, the DRX volume fraction is insignificant (< 1.5%) for most of the samples and therefore is not shown in Fig. 7. Above T_β, it distinctly rises with increasing deformation temperature and decreasing strain rate. At 1223 K, the extent of increase with decreasing strain rate (from 1 s^{-1} to 0.01 s^{-1}) is 24%, while it is 14% for deformation at 1173 K. The evolution of recrystallized grain size of samples deformed above T_β is shown in Fig. 8a. A good correlation of the size d_r and ln Z is found above T_β (Fig. 8b). The experimental relationship can be expressed as:

$$d_r = -7.3 \ln Z + 178.6 \quad (5)$$

The size of the recrystallized grains rises with increasing deformation temperature and decreasing deformation rate.

After deformation at 1223 K and a strain rate of 0.1 s^{-1}, only a small amount of recrystallized grains is formed. In addition, CDRX takes place (Fig. 9). As shown in Fig. 9,

some small grains are formed along prior β-grain boundaries. The orientation of the recrystallized grains (1 to 5) is demonstrated by three-dimensional graphics (Fig. 9a) and PFs (Fig. 9b). The misorientation across a prior grain is given in Fig. 9c. In Fig. 9b the upper and lower {100} and {111} PFs show the orientations of two prior β-grains and the small recrystallized grains (1 - 5), respectively. From Figs. 9a and b it is found that the recrystallized grains are rotated from prior β-grains by different amounts. Apparently, there is a cumulative misorientation from center to edge of the deformed grains (Fig. 9c).

Figure 10 shows DRX grains (in blue color) as defined by GOS in samples deformed with a strain rate of 0.01 s^{-1} at 1223 K ((a) - (c)) and 1173 K ((d) - (f)). The majority of DRX grains exist in the vicinity of HAGBs of prior β-grains.

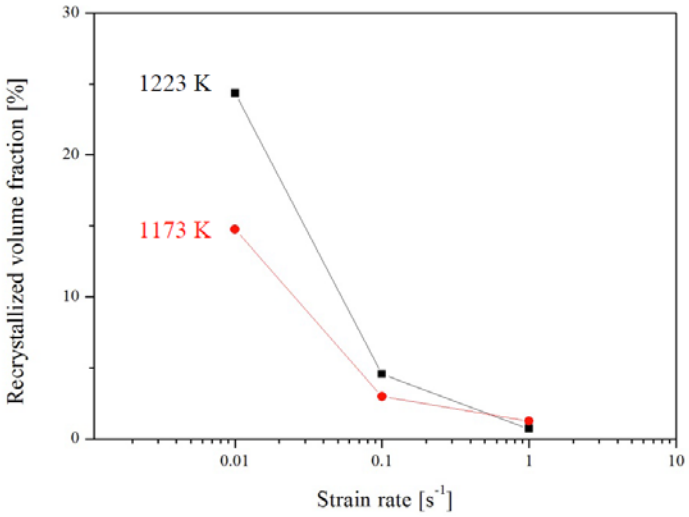

Fig. 7: Recrystallized volume fraction as a function of strain rate for samples hot-compressed above T_β.

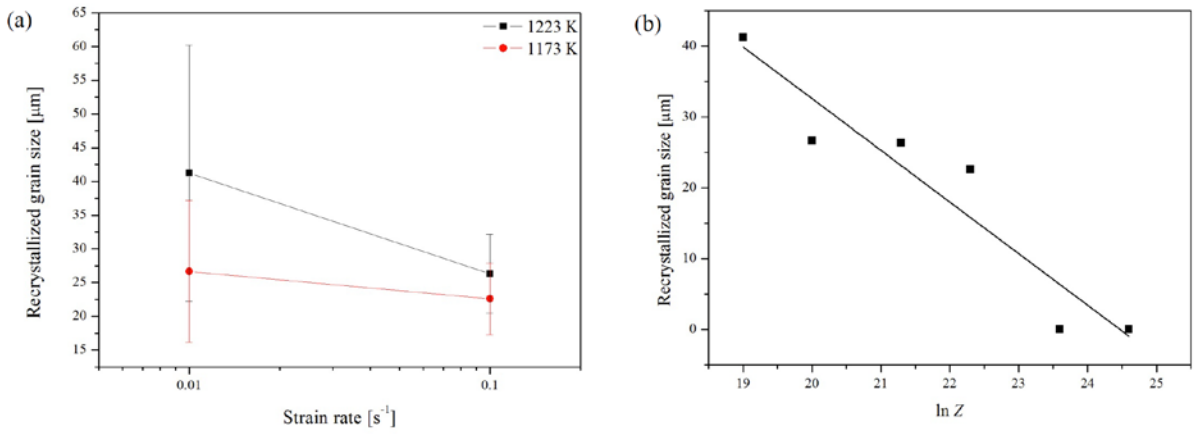

Fig. 8: Size of recrystallized grains as a function of strain rate (a) and ln *Z* (b) for samples hot-compressed above T_{β}.

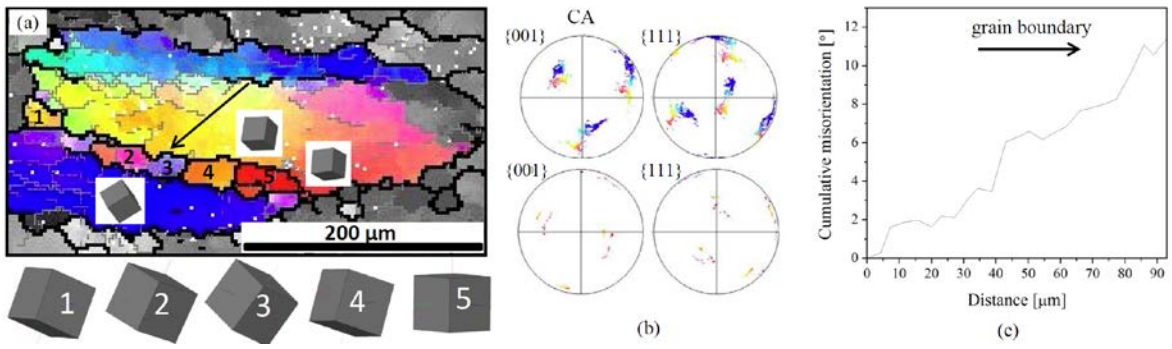

Fig. 9: (a) EBSD CA-IPF map of Ti5321 alloy hot-compressed to a strain of 60% at 1223 K and a strain rate of 0.1 s^{-1} (white framed area in Fig. 5 b). In (b) PFs present the orientation data of some selected colored grains. The upper and lower PFs present the orientations of two prior β-grains and the recrystallized grains 1 to 5, respectively. (c) shows the point-to-origin misorientation along the black arrow towards the lower HAGB. (sample reference system as in Fig. 1)

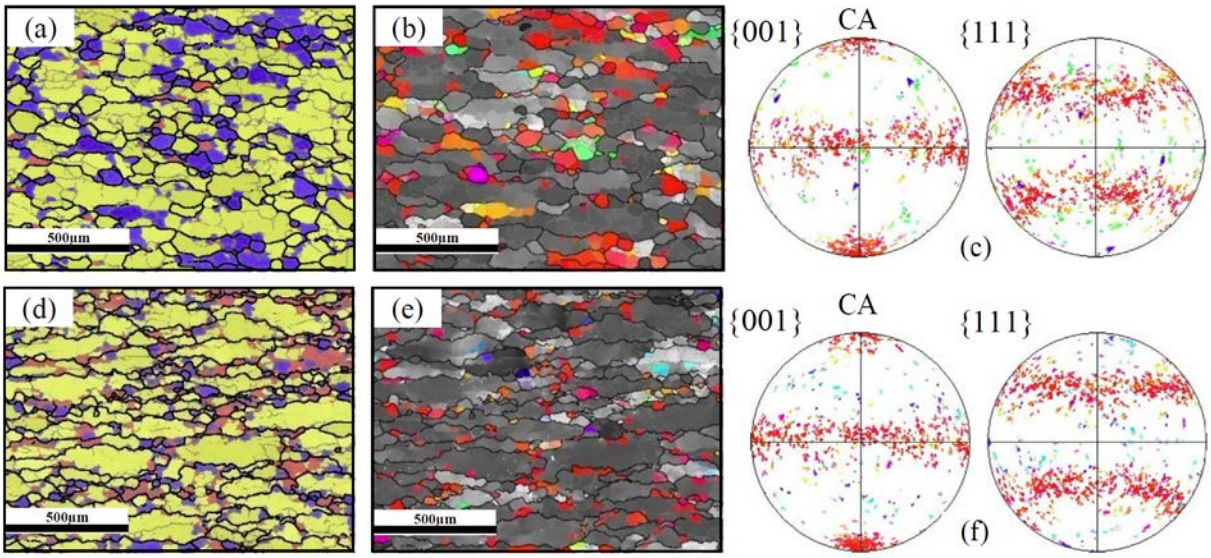

Fig. 10: DRX grains separated by the GOS method (in blue color) in samples deformed at a strain rate of 0.01 s^{-1} (a, d) with corresponding CA-IPF mappings (b, e) and {100} and {111} PFs (c, f). The deformation temperature is 1223 K (a to c) and 1173 K (d to f). (sample reference system as in Fig. 1)

The dominant red and blue color after all hot-deformation conditions in Fig. 5 reveals a <100> <111> double-fiber texture (<100> and <111> preferentially oriented parallel to CA). Fig. 11 shows the corresponding {100} PFs. A quantitative analysis of both fibers is shown in Fig. 12.

Above T_β, the volume fraction of the <100> fiber decreases with decreasing temperature, while for <111> it is increasing (Fig. 12a). In parallel the same behavior should be observed for increasing strain rate, but it is only seen for <111>. Plotting the volume fraction vs. ln Z yields a decreasing trend for <100> and an increasing one for <111> (Fig. 12b). In the (α + β)-phase field, the volume fraction of the <100> fiber follows the same trend with ln Z as in the β-phase field (Fig. 12b). In contrast, <111> does not increase further, but instead shows a larger spread. It should be noted that texture measurements with EBSD are hard to fulfill the necessary grain statistics and therefore the trends described should be treated with care.

	0.01 s^{-1}	0.1 s^{-1}	1 s^{-1}
1223 K	(a) ln Z = 19.0	(b) ln Z = 21.3	(c) ln Z = 23.6
	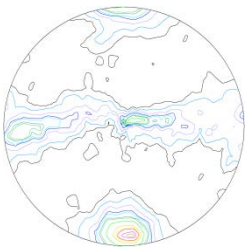	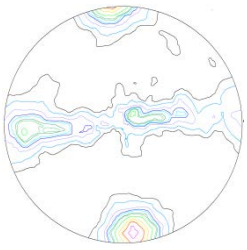	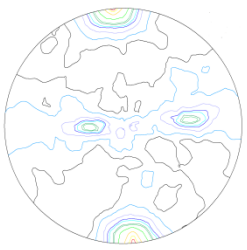
1173 K	(d) ln Z = 20.0	(e) ln Z = 22.3	(f) ln Z = 24.6
	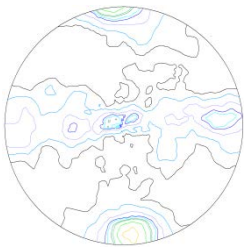	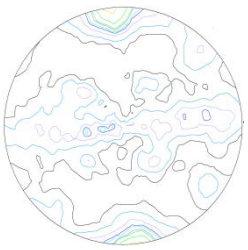	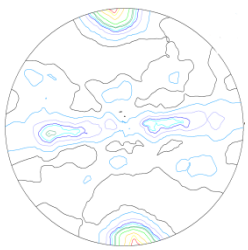
1103 K	(g) ln Z = 35.7	(h) ln Z = 38.0	(i) ln Z = 40.3
	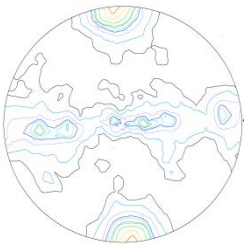	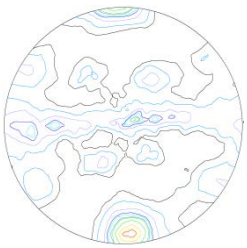	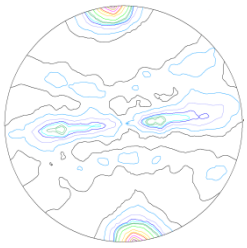
1073 K	(j) ln Z = 36.9	(k) ln Z = 39.1	(l) ln Z = 41.5
	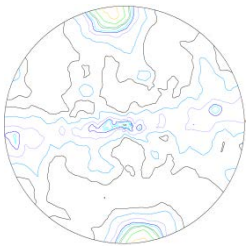	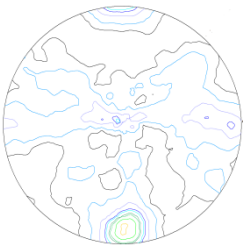	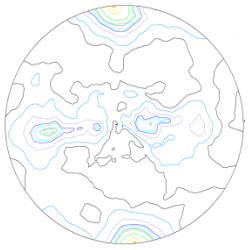
1023 K	(m)ln Z = 38.9	(n) ln Z = 41.2	(o) ln Z = 43.5
	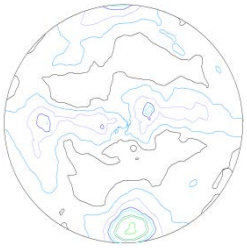		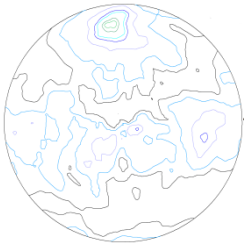

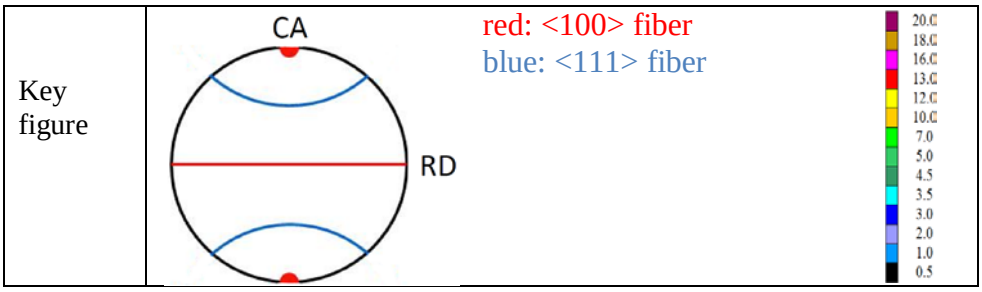

Fig. 11: {100} PFs of the β-phase in Ti5321 following hot-compression at different strain rates and temperatures.

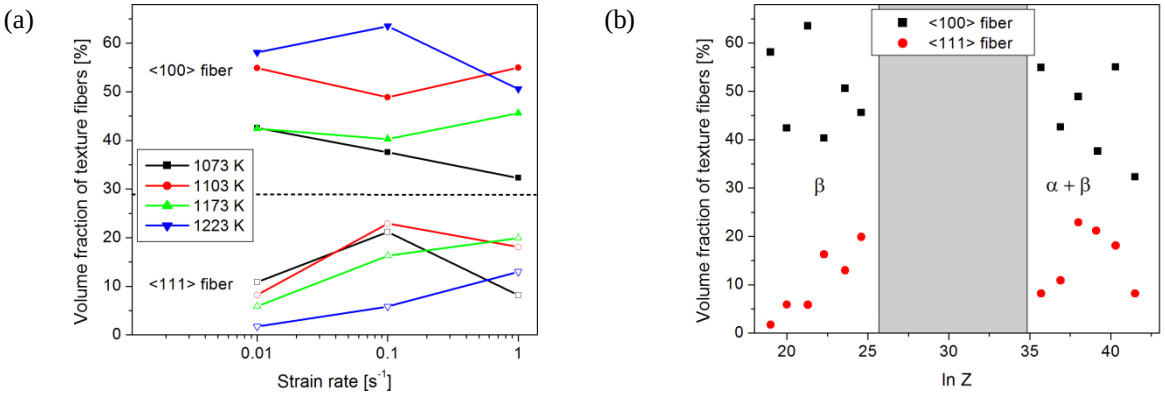

Fig. 12: Volume fraction of <100> and <111> texture fibers as a function of strain rate at different temperatures (a) and Z parameter (b) for hot-compressed samples. The shaded area in (b) is bordered by the maximum and minimum ln Z value for T_β in the β- and ($\alpha + \beta$)-phase field, respectively.

3.5. Characteristics of α-phase and micro-hardness

Below T_β, the DRX volume fraction is insignificant (< 1.5%) for most of the samples and therefore is not shown in Fig. 7.

Figure 13 shows CA-IPF maps of the α-phase in samples deformed at 1023 K and 1073 K at different strain rates. The volume fraction of the α-phase is smaller at 1073 K than at 1023 K, and microstructural evolution of the α-phase at different strain rates below T_β shows a similar trend. Therefore, in Fig. 13 at 1073 K, the CA-IPF map of the α-phase is shown only for a

strain rate of 0.01 s^{-1}. Fig. 14 shows mean values of the microstructural features of α-grains in samples hot-compressed at 1023 K. The α-grains do not indicate significant differences in their size and shape at any strain rate.

The micro-hardness after different deformation conditions is shown in Fig. 15. It is obvious that the micro-hardness of samples hot-compressed at 1023 K and 1073 K is higher than that of samples compressed at higher temperatures. At the lowest temperature of 1023 K, the micro-hardness increases with increasing strain rate, while for the rest it is almost independent. It is interesting that above 1103 K the micro-hardness is almost constant.

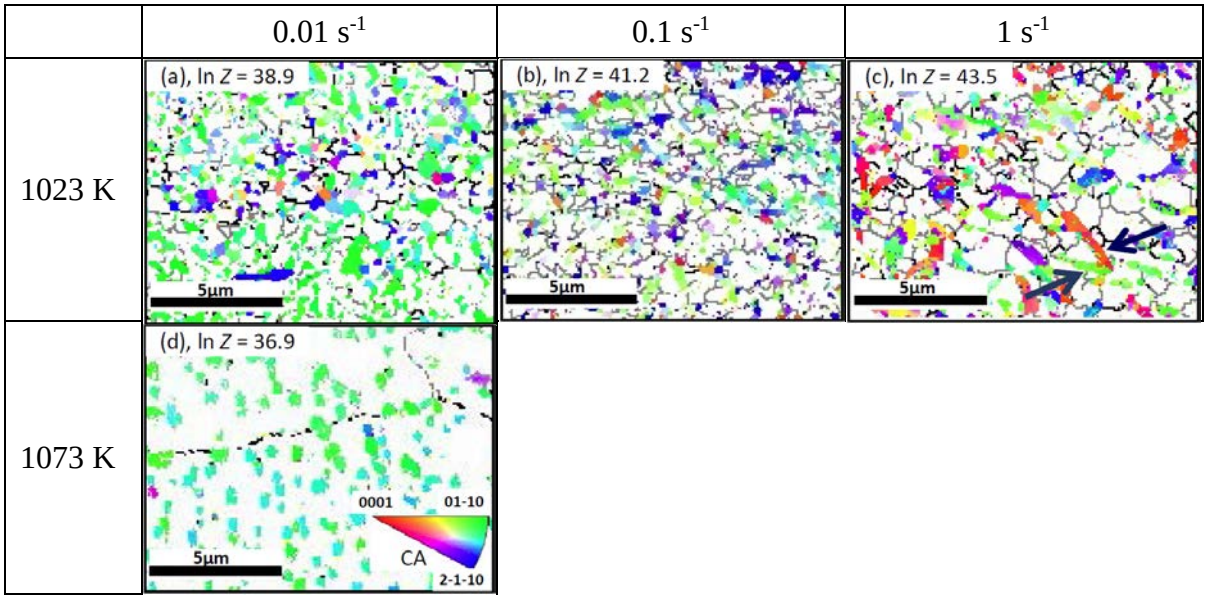

Fig. 13: EBSD CA-IPF maps of the α-phase in samples hot-compressed at different temperatures and strain rates, respectively ln *Z*. LAGBs and HAGBs of the white β-phase are gray and black, respectively. (sample reference system as in Fig. 1)

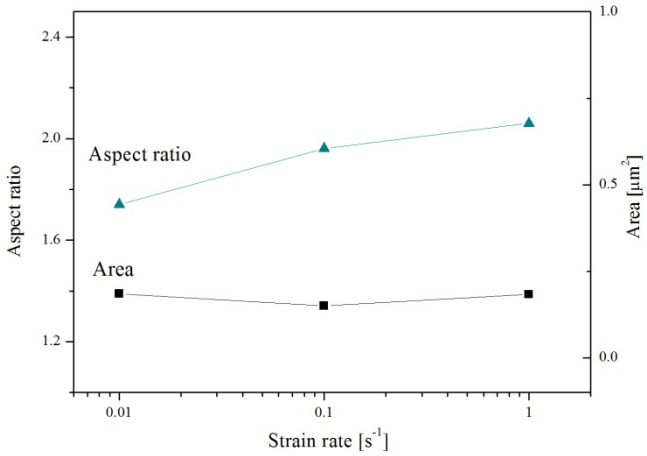

Fig. 14: Mean values of the microstructural features (aspect ratio and size (area)) of α-grains in samples hot-compressed at 1023 K.

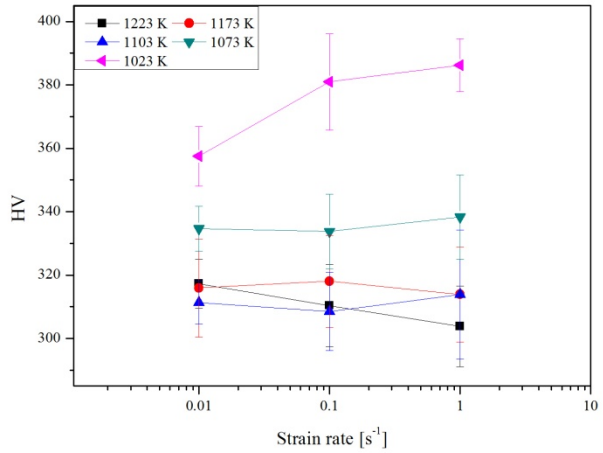

Fig. 15: Micro-hardness of samples deformed under different deformation conditions.

4. Discussion

The differences in flow behavior above T_β indicate two distinct deformation mechanisms. The flow curves for $\dot{\varepsilon} = 0.01$ s^{-1} at 1223 K and 1173 K exhibit a quick rise of the stress to a plateau and subsequent steady state flow. This behavior is characteristic for DRV balancing work-hardening during deformation [20]. Work-hardening is due to dislocation multiplication and interaction, while DRV takes place by climb and/or cross-slip of edge and/or screw dislocations, respectively [14, 20]. DRV was reported as the dominant restoration mechanism

in many β-Ti alloys, such as Ti1023, Ti5553 and Ti55531 [2, 18, 19].

Different deformation mechanisms were found depending on deformation temperature and strain rate, most suitably characterized by Z. At the lowest possible temperature above T_β and highest strain rate (T = 1173 K and $\dot{\varepsilon}$ = 1 s^{-1}, ln Z = 24.6), work-hardening dominates, whereas at the highest temperature above T_β and lowest strain rate (T = 1223 K and $\dot{\varepsilon}$ = 0.01 s^{-1}, ln Z = 19.0) DRV prevails. Similar observations were reported for other metals (e.g. Ni and Cu). In general, the shape of the flow curves changes with Z indicating a change in deformation behavior [16].

Small stress oscillations are observed in Figs. 2a and b for $\dot{\varepsilon}$ = 1 s^{-1}. Such a serrated flow behavior, but with decreasing amplitude with increasing strain, is generally associated with DRX at low strain rates and high temperatures (low Z value) [15, 20]. A transition from single peak to multiple peaks happens with decreasing strain rate [16]. However, in this study multiple peaks are observed at high strain rate, and the volume fraction of DRX is very low (<5%) as shown in Figs. 5 and 7. Thus, the stress oscillations in the flow curves may not be related to DRX, but, very likely are the result of a control problem of the thermomechanical simulator at high strain rate.

Additional information on the deformation mechanism is provided by the activation energy Q estimated. In the present case, Q in the β-phase field is higher than that reported for Ti self-diffusion in the pure β-phase (153 kJ/mol) [30]. The difference has been attributed to the influence of alloying elements [31]. The break-up of α-platelets during isothermal deformation leads to an increase of the activation energy. This was confirmed in Ti5553. The activation energy of 183 kJ/mol reported for Ti5553 with the (α+β)-phase being the initial microstructure deformed in the (α+β)-phase field is lower than that of the same alloy with a pure β-phase as initial microstructure [2, 10]. The Q value obtained in the (α+β)-phase field is higher than that found for Ti1023 (294 kJ/mol) [29], Ti55531 (275 kJ/mol) [18] and Ti5553 (183 kJ/mol) [2]. This may be due to the comprehensive effect of amount, morphology and

dynamic globularization of the α-phase [10, 18, 31].

4.1. Dynamic recrystallization

After hot-deformation the microstructure of metals has been found to depend on Z [16, 20]. In this work, this dependence is discussed on samples compressed above T_β. Z influences the cell and subgrain structure and, thus, affects DRX. A good correlation of the size of recrystallized grains and ln Z has been found (Fig. 8b).

The evolution of microstructure can be explained as follows. It has been reported that DRV plays an important role during DRX, especially in the early stage of recrystallization [19, 32]. At temperatures just above T_β and high strain rates (T = 1173 K, $\dot{\varepsilon}$ = 1 s^{-1}, ln Z = 24.6, Fig. 6f), a three-dimensional subgrain structure is found. Such a dislocation arrangement usually starts close to HAGBs, where the dislocation density is typically higher than in the grain interior. It has been discussed above that at this deformation condition work-hardening still dominates, however, the mobility of HAGBs is low. As a result, almost no recrystallized grains are found. With decreasing Z, enabled by the lower strain rate and higher temperature, HAGBs of the original grains bulge into the neighboring subgrain structure (Fig. 6b) [20], while at the lowest Z (T = 1223 K, $\dot{\varepsilon}$ = 0.01 s^{-1}, ln Z = 19) the deformation is dominated by DRV (Fig. 6a). As demonstrated in Fig. 10, HAGBs are bulging, while LAGBs are observed in the grain interior. The subgrains remain equiaxed and coarsen. This is a typical DRV microstructure caused by dislocation climb and cross-slip. The bulging mechanism of HAGBs leads to a volume fraction of recrystallized grains larger than that in samples with higher Z.

CDRX was observed at an intermediate strain rate of 0.1 s^{-1} (T = 1223 K, ln Z = 21.3, Fig. 9). In Ti55531, CDRX was observed at a strain rate of 1 s^{-1} after a strain of 50% [17]. CDRX is not dominant at low strain rates, but with increasing strain rate CDRX becomes more important along with DDRX [18].

There is no nucleation and growth stage for CDRX. Instead, it can be described as a

progressive rotation of subgrains adjacent to preexisting grain boundaries leading to the transformation of LAGBs into HAGBs [33, 34]. Conventionally, CDRX is characterized by cumulative misorientation from center to edge of prior grains [8, 14]. It is obvious that during CDRX recrystallized grains are rotated by different degrees with regard to prior grains, while the old grains develop a gradient of misorientation from center to edge (Fig. 9). This gradient is accommodated by geometrically necessary dislocations arranged in subgrain boundaries [17]. New grains with HAGBs form at higher strains near prior β-grain boundaries by progressive rotation of subgrains with little accompanying boundary migration. This is a strain-induced phenomenon [20].

4.2. Texture

As shown in Fig. 11, the axisymmetric texture developed during hot-compression is a <100> <111> double-fiber texture. Similar observations were reported for Ti-5Al-5Mo-5V-1Cr-1Fe (Ti55511) [35] and other bcc materials [36, 37]. The <100> <111> double-fiber texture was forecasted as stable texture after compressive deformation by Barrett et al. based on the theories that three most stressed slip systems ({110}<111>, {112}<111>, or {123}<111>) are activated in bcc structures with stable orientation remaining during forging [38].

In the β-phase field, the volume fraction of the <100> fiber within the spread of data slightly decreases with ln *Z*. This can be explained with DRX. As shown in Fig. 7, the DRX volume fraction increases with decreasing strain rate and increasing temperature. The PFs in Fig. 10 indicate that the DRX grains predominantly exhibit orientations of the <100> fiber. The majority of subgrains and DRX grains form in the vicinity of grain boundaries of prior β-grains. As a consequence, with decreasing strain rate the grain boundaries become more and more serrated. As discussed in section 4.1, HAGB bulging is driven by the reduction of the dislocation density, i.e. reduction of stored energy during hot-compression. The formation of

DRX grains with <100> fiber orientation begins with HAGB bulging. During growth they replace other orientations (including grains belonging to the <111> fiber). It was reported that slip systems {112}<111> and {123}<111>, both lead to <100> and <111> fiber textures, whereas the {110}<111> slip system leads to a strong <111> fiber. This replacement may be attributed to the low activity of {110}<111> slip which weakens the <111> and strengthens the <100> fiber [39]. A similar recrystallization behavior was reported for Ti55511 [35]. In contrast, the volume fraction of the <111> fiber linearly increases with ln *Z*. As analyzed above, work-hardening prevails at high *Z* whereas dynamic recovery dominates at low Z. It is understandable that dislocation slip along the <111> direction on the {110} slip plane during work-hardening contributes to lattice rotation towards the stable compression texture components, thus generally increasing the intensity of the <111> fiber. As a result, the formation of the <111> fiber texture is dominated by deformation and not by DRX.

In the (α + β)-phase field texture formation by dislocation slip and DRX is influenced by the α-precipitation. While the general trend of the <100> fiber is not changed, the <111> fiber is affected strongly. It has been reported that β slip system activity leading to texture development can be affected by dislocation slip transmission across the α/β interface which is related to the orientation relationship between α- and β-phase [39]. However, because of the spread of data in this study, speculation about the change of mechanisms of texture formation will not be given. To shed more light on this problem, statistically more reliable texture measurements with synchrotron and neutron radiation are under way.

4.3. α-phase

Figure 13 shows CA-IPF maps for the α-phase in samples deformed at 1023 K at different strain rates. The α-grains do not show a significant change in size and shape with changing strain rate. This agrees with results reported for Ti5333 and Ti55531 [2, 18]. Therefore, it can be concluded that dynamic globularization of the α-phase is not much affected by the strain

rate, but rather by strain [32]. Fig. 14 indicates that at the same temperature of 1023 K the aspect ratio of α-grains slightly decreases with decreasing strain rate. Black arrows in Fig. 13c point out the existence of some elongated α-grains. It was reported that the dynamic globularization process of the elongated α-phase occurs by fragmentation via DRV followed by break-up through penetration of the β-phase along the α-HAGBs [32]. Consequently, since the deformation at higher strain rates affects the formation of LAGBs and HAGBs it may as well affect the dynamic globularization process of the α-phase. Another reason may be that at higher stain rates dynamic globularization is not completed due to less deformation time. During dynamic globularization the penetration of the β-phase into the α-phase is a diffusion-controlled process [40], i.e. higher deformation temperature and more time will promote globularization. This may also explain why the aspect ratio of α-grains at a strain rate of 0.01 s^{-1} slightly decreases with increasing deformation temperature (Fig. 14).

The micro-hardness is related to the volume fraction, size and shape of α-precipitates [1]. In this work, the size and shape does not seem to play a role because of negligible change in area and aspect ratio (Fig. 14). The micro-hardness is inversely related to the volume fraction of equiaxed α-phase [1], which for the samples deformed at lower strain rate is higher than for those deformed at higher strain rate at the same deformation temperature (Figs. 13 a-c). As a result, the micro-hardness increases with increasing strain rate. Another reason may be the degree of dislocation multiplication and interaction being more intense at high than at low strain rate, while the degree of flow softening is similar (Fig. 2). As a result, the density of dislocations is higher in the sample deformed at higher strain rate.

The pinning of dislocations at α-phase boundaries locally increases the dislocation density, which promotes DRX of β-grains [41]. As the volume fraction of the primary α-phase is higher in samples compressed at 1023 K than at 1073 K, apparently, there are more fine DRX β-grains in samples deformed at lower temperature. This may explain their higher extent of flow softening.

5. Conclusions

Hot-compression of the metastable Ti5321 across T_β was studied in detail. The resulting deformation behavior and microstructure and texture development were correlated with deformation temperature and strain rate via the Zener-Hollomon parameter *Z*. The main conclusions from this work are as follows:

1. Besides work-hardening DRV and DRX is found. At high *Z*, work-hardening is more important, whereas DRV and CDRX become dominant at low *Z*. The activation energy for hot-compression of Ti5321 amounts to 240 kJ/mol and 370 kJ/mol in the β- and (α+β)-phase field, respectively.
2. A <100> <111> double-fiber texture is found for most deformation conditions. In the β-phase field, the volume fraction of the <100> fiber slightly decreases, while that of <111> clearly increases with increasing ln *Z*. The <100> fiber texture is mainly associated with DRX. In the (α+β)-phase field, texture formation is influenced by α-precipitation. No clear trend is observed for the <111> fiber.
3. Deformation temperature and strain rate do not significantly affect the dynamic globularization process of the α-phase. DRX β-grains forming in the (α+β)-phase field are associated with the dynamic globularization process of the α-phase and affect the flow softening behavior.

Acknowledgments

The authors are grateful for financial support through the International Science and Technology Cooperation Program of China (2015DFA51430), 111 Project (B17002).

6. References

[1] G. Lütjering, J.C. Williams, Titanium, 2nd ed., Springer, Berlin, 2007.

[2] N.G. Jones, R.J. Dashwood, D. Dye, M. Jackson, Thermomechanical processing of Ti-

5Al-5Mo-5V-3Cr, Mater. Sci. Eng. A 490 (2008) 369-377.

[3] D. Banerjee, J.C. Williams, Perspectives on titanium science and technology, Acta Mater. 61 (2013) 844-879.

[4] S.K. Jha, K.S. Ravichandran, High-cycle fatigue resistance in β-titanium alloys, JOM 52 (2000) 30-35.

[5] N.P. Gurao, S. Suwas, Study of texture evolution in metastable β-Ti alloy as a function of strain path and its effect on α transformation texture, Mater. Sci. Eng. A 504 (2009) 24-35.

[6] M. Premkumar, V.S. Himabindu, S. Banumathy, A. Bhattacharjee, A.K. Singh, Effect of mode of deformation by rolling on texture evolution and yield locus anisotropy in a multifunctional β titanium alloy, Mater. Sci. Eng. A 552 (2012) 15-23.

[7] S. Banumathy, R.K. Mandal, A.K. Singh, Texture and anisotropy of a hot rolled Ti-16Nb alloy, J. Alloys Compd. 500 (2010) L26-L30.

[8] H.J. McQueen, Development of dynamic recrystallization theory, Mater. Sci. Eng. A 387-389 (2004) 203-208.

[9] J.K. Fan, H.C. Kou, M.J. Lai, B.Tang, H. Chang, J.S. Li, Hot deformation mechanism and microstructure evolution of a new near β titanium alloy, Mater. Sci. Eng. A 584 (2013)121-132.

[10] H. Matsumoto, M. Kitamura, Y.P. Li, Y. Koizumi, A. Chiba, Hot forging characteristic of Ti-5Al-5V-5Mo-3Cr alloy with single metastable β microstructure, Mater. Sci. Eng. A 611(2014)337-344.

[11] A. Samiee, G. Casillas, M. Ahmed, D.G. Savvakin, R. Naseri and E. Pereloma, Formation of deformation-induced products in a metastable β-titanium alloy during high temperature compression. Metals 8 (2018) 100.

[12] M. Jackson, N.G. Jones, D. Dye, R.J. Dashwood, Effect of initial microstructure on plastic flow behaviour during isothermal forging of Ti-10V-2Fe-3Al, Mater. Sci. Eng. A

501 (2009) 248-254.

[13] H.C. Kou, Y. Chen, B. Tang, Y.W. Cui, F. Sun, J.S. Li, X.Y. Xue, An experimental study on the mechanism of texture evolution during hot-rolling process in a β titanium alloy, J. Alloys Compd. 603 (2014) 23-27.

[14] T. Sakai, A. Belyakov, R. Kaibyshev, H. Miura, J.J. Jonas, Dynamic and post-dynamic recrystallization under hot, cold and severe plastic deformation conditions, Prog. Mater. Sci. 60 (2014) 130-207.

[15] D.G. Cram, H.S. Zurob, Y.J.M. Brechet, C.R. Hutchinson, Modelling discontinuous dynamic recrystallization using a physically based model for nucleation, Acta Mater. 57 (2009) 5218-5228.

[16] M. Hasegawa, M. Yamamoto, H. Fukutomi, Formation mechanism of texture during dynamic recrystallization in γ-TiAl, nickel and copper examined by microstructure observation and grain boundary analysis based on local orientation measurements, Acta Mater. 51 (2003) 3939-3950.

[17] X.G. Fan, Y. Zhang, P.F. Gao, Z.N. Lei, M. Zhan, Deformation behavior and microstructure evolution during hot working of a coarse-grained Ti-5Al-5Mo-5V-3Cr-1Zr titanium alloy in beta phase field, Mater. Sci. Eng. A 694 (2017) 24-32.

[18] F. Warchomicka, C. Poletti, M. Stockinger, Study of the hot deformation behaviour in Ti-5Al-5Mo-5V-3Cr-1Zr, Mater. Sci. Eng. A 528 (2011) 8277- 8285.

[19] J. Zhao, J. Zhong, F.Yan, F. Chai, M. Dargusch, Deformation behaviour and mechanisms during hot compression at supertransus temperatures in Ti-10V-2Fe-3Al, J. Alloys Compd. 710 (2017) 616-627.

[20] F.J. Humphreys, M. Hatherly, Recrystallization and Related Annealing Phenomena, 2nd ed., Elsevier, Oxford, 2004.

[21] B. Sander, D. Raabe, Texture inhomogeneity in a Ti-Nb-based β-titanium alloy after warm rolling and recrystallization, Mater. Sci. Eng. A 479 (2008) 236-247.

[22] J.Q. Zhang, H.S. Di, H. T. Wang, K. Mao, T.J. Ma, Y. Cao, Hot deformation behavior of Ti-15-3 titanium alloy: a study using processing maps, activation energy map, and Zener–Hollomon parameter map, J. Mater. Sci. 47 (2012) 4000-4011.

[23] Y.Q. Zhao, C.L Ma, H. Chang, S.W. Xin, L. Zhou, New high strength and high toughness titanium alloy with 1200 MPa, Mater. China, 35 (2016) 914-918. (In Chinese)

[24] B. Gu, P. Chekhonin, R. Schaarschuch, C.-G. Oertel, S.W. Xin, C.L. Ma, L. Zhou, W.M. Gan, W. Skrotzki, Microstructure, texture and hardness of a metastable β-titanium alloy after bar-rolling and annealing, J. Alloys Compd. 825 (2020) 154082.

[25] S.I. Wright, M.M. Nowell, D.P. Field, A review of strain analysis using electron backscatter diffraction, Microsc. Microanal. 17 (2011) 316-329.

[26] A.A. Gazder, M. Sanchez-Araiza, J.J. Jonas, E.V. Pereloma, Evolution of recrystallization texture in a 0.78 wt.% Cr extra-low-carbon steel after warm and cold rolling, Acta Mater. 59 (2011) 4847-4865.

[27] X.Q. Yin, C.H. Park, Y.F. Li, W.J. Ye, Y.T. Zuo, S.W. Lee, J.T. Yeom, X.J. Mi, Mechanism of continuous dynamic recrystallization in a 50Ti-47Ni-3Fe shape memory alloy during hot compressive deformation, J. Alloys Compd. 693 (2017) 426-431.

[28] C.M. Sellars, W.J. McG. Tegart, On the mechanism of hot deformation, Acta Metall.14 (1966) 1136-1138.

[29] D.G. Robertson, H.B. McShane, Analysis of high temperature flow stress of titanium alloys IMI 550 and Ti-10V-2Fe-3AI during isothermal forging, Mater. Sci. Technol. 14 (1998) 339-345.

[30] I. Weiss, S.L. Semiatin, Thermomechanical processing of beta titanium alloys – an overview, Mater. Sci. Eng. A 243 (1998) 46-65.

[31] M. Dikovits, C. Poletti, and F. Warchomicka, Deformation mechanisms in the near-β titanium alloy Ti-55531, Met. Mater. Trans. A, 45 (2014) 1586-1596.

[32] L. Li, J. Luo, J.J. Yan, M.Q. Li, Dynamic globularization and restoration mechanism of

Ti-5Al-2Sn-2Zr-4Mo-4Cr alloy during isothermal compression, J. Alloys Compd. 622 (2015) 174-183.

[33] J.K. Solberg, H.J. McQueen, N. Ryum, E. Nes, Influence of ultra-high strains at elevated temperatures on the microstructure of aluminium. Part I, Phil. Mag. A, 60 (1989) 447-471.

[34] S. Gourdet, F. Montheillet, A model of continuous dynamic recrystallization, Acta Mater. 51 (2003) 2685-2699.

[35] K. Li, P. Yang, The formation of strong {100} texture by dynamic strain-induced boundary migration in hot compressed Ti-5Al-5Mo-5V-1Cr-1Fe alloy, Metals 7 (2017) 412.

[36] O. Engler, V. Randle, Introduction to Texture Analysis: Macrotexture, Microtexture, and Orientation Mapping, 2nd ed., CRC Press, Taylor & Francis Group, Boca Raton, 2010.

[37] S. Primig, H. Leitner, W. Knabl, A. Lorich, H. Clemens, R. Stickler, Textural evolution during dynamic recovery and static recrystallization of molybdenum. Metall. Mater. Trans. A (2012) 43, 4794-4805.

[38] C.S. Barrett, T.B. Massalski, Structure of metals, McGraw-Hill, New York, 1966.

[39] L. Meng, T. Kitashima, T. Tsuchiyama, and M. Watanabe, β-Texture evolution during a precipitation in the two-step forging process of a near-β titanium alloy, Metall. Mater. Trans. A (2020) 51A, 5112-5122.

[40] S. Roy, S. Suwas, The influence of temperature and strain rate on the deformation response and microstructural evolution during hot compression of a titanium alloy Ti-6Al-4V-0.1B, J. Alloys Compd. 548 (2013) 110-125.

[41] Y. Chen, J.S. Li, B. Tang, H.C. Kou, X.Y. Xue, Y.W. Cui, Texture evolution and dynamic recrystallization in a beta titanium alloy during hot-rolling process, J. Alloys Compd. 618 (2015) 146-152.